Characterisation of Solid Oxide Fuel Cell Ni–8YSZ substrate by synchrotron X-ray nano-tomography: from 3D reconstruction to microstructure quantification

J. Laurencin [a,*], R. Quey [b], G. Delette [a], H. Suhonen [c], P. Cloetens [c], P. Bleuet [b]

[a] CEA-Liten, 17 rue des martyrs, 38054 Grenoble Cedex 9, France
[b] CEA-Leti, MINATEC Campus, 17 rue des martyrs, 38054 Grenoble Cedex 9, France
[c] European Synchrotron Radiation Facility, BP 220, 38043 Grenoble, France

ABSTRACT

A methodology, based on synchrotron X-ray nano-tomography measurements, is proposed to obtain 3D reconstructions of porous supports for Solid Oxide Fuel Cell (SOFC). The methodology has been applied to investigate the microstructure of a typical Ni–8YSZ cermet substrate of an Anode Supported Cell (ASC). Experimental conditions have been optimised so that a 3D reconstruction of $42\,\mu m \times 42\,\mu m \times 105\,\mu m$ has been computed with a voxel size of 60 nm.

The 3D reconstruction has been numerically analysed showing a quasi isotropy over the medium. A special attention has been paid to compute the morphological properties controlling the gas diffusion through the support. In this frame, it has been found that a volume as large as $35\,\mu m \times 35\,\mu m \times 35\,\mu m$ is required to be statistically representative for the whole substrate. More particularly, the tortuosity factor τ has been calculated on the basis of finite element simulations. The effect of the boundary conditions taken for these simulations has been investigated. In the direction perpendicular to the anode/electrolyte interface, the tortuosity factor has been determined to $\tau_z = 2.8^{+0.3}_{-0.2}$.

1. Introduction

Solid Oxide Fuel Cells (SOFCs) are electrochemical devices that ensure the conversion of fuel chemical energy into electricity at high temperature. Since they present high efficiencies and large fuel flexibility, SOFCs appear as an attractive technology for economic power generation. The active part of SOFC corresponds to a three-layered structure, constituted by a dense electrolyte sandwiched between two porous electrodes. The most common materials used for this membrane are Lanthanum Strontium Manganite (LSM) for the cathode, Yttria Stabilized Zirconia (YSZ) for the electrolyte, and Nickel/YSZ cermet (Ni–YSZ) for the anode.

Nowadays, efforts are ongoing to operate the SOFCs at intermediate temperature ($T \le 800\,^{\circ}C$) in order to reduce the material costs and simultaneously improve the cell reliability. Anode Supported Cells (ASCs) have been designed for such application [1,2]. The ASC configuration is based on a thick highly porous anodic substrate, on which a thin electrolyte and the functional electrodes are layered. The substrate, which is used as the cell structural support, presents a coarse microstructure to facilitate the gas transportation; whereas the fine microstructure of the functional layer is optimised for the electrochemical reactions [3,4]. Thanks to its configuration, ASC allows reducing the ohmic losses in the electrolyte and exhibits high power densities. Furthermore, it has been shown that this design is well adapted to operate with natural gas [5].

However, the microstructure features of the electrodes are key parameters which determine the cell polarization resistance, and hence, the electrochemical performances [6–8]. The evolution of these microstructure parameters after a long term operation or after redox cycling could also explain the degradation in electrochemical performances [9–12].

More particularly, it has been shown that gas diffusion into the ASC substrate can induce high concentration overpotentials, which can limit the cell efficiency for operation at elevated current density [13,14]. It is worth noting that the gas transport up to the electrochemical active sites is controlled by the morphological properties of the electrode supports [7,15], more particularly by the 3D topology of the pores network. These parameters also affect the methane conversion rate for SOFC operating under direct internal reforming [16]. As a consequence, the knowledge of these structural properties is essential to predict the mass transport into the porous substrate which is linked to the ASC efficiency.

For all these reasons, several efforts have been recently paid (i) to obtain 3D reconstructions of real electrodes and (ii) to characterise their morphological and fluid properties [11,17–29]. Focused Ion Beam coupled with a Scanning Electron Microscope (FIB-SEM)

* Corresponding author. Tel.: +33 4 38782210; fax: +33 4 38784139.
 E-mail address: laurencin@chartreuse.cea.fr (J. Laurencin).

[11,17–25] and X-ray nano-tomography [26–29] methods have been widely employed for this purpose. It has been demonstrated that both techniques, radically different in their basic principles, stand to obtain 3D reconstruction of relatively small volume (typically close to $10\,\mu m \times 10\,\mu m \times 10\,\mu m$ [23]) at high resolution (as low as 10 nm for FIB-SEM technique [11] and 45 nm for X-ray tomography [29]). They have been successfully applied to determine the microstructure properties of functional electrodes. Because of the fine microstructure of such layers, it has been shown that the volumes of the reconstructions are sufficiently large to reach a Representative Volume Element (RVE) of the analysed medium [18–20]. For instance, Wilson et al. [18] have stated that the analysis of volumes higher than $>500\,\mu m^3$ are sufficient to provide microstructure properties that are representative for the overall electrode. This result is confirmed by Cronin et al. [19] who suggested that volumes of $\sim 1000\,\mu m^3$ are large enough to provide good statistics. These volumes appear to be slightly lower than the one recommended by Metcalfe et al. [30]: by a numerical approach, these authors have established that the size of the domain should be 14 times the mean particles diameter to adequately represent the electrode structure. It can be noticed that Joos et al. [24] have succeeded to reconstruct the entire cathode thickness of an ASC (volume of $30.7\,\mu m \times 5.25\,\mu m \times 15.75\,\mu m$ obtained by FIB-SEM). The largest reconstruction was achieved by Kanno et al. [25] for a conventional Ni–YSZ anode deposited onto a thick electrolyte: the authors have investigated a reconstructed structure as large as $45.8\,\mu m \times 14.5\,\mu m \times 26.2\,\mu m$. However, at this time, no study has been devoted to the ASC substrate, probably because its coarse microstructure requires an analysis over a larger volume.

The present study aims at overcoming this limitation and is dedicated to the reconstruction of a standard Ni–ZSZ cermet support. For this purpose, hard X-ray nano-tomography has been used to obtain valuable 3D imaging of the microstructure at a relevant scale. The 3D reconstruction has been analysed by using computational modelling in order to determine the morphological properties controlling the gas diffusion in the substrate. These parameters correspond to the fluid contiguity, the porosity, the mean pore radius and the tortuosity factor.
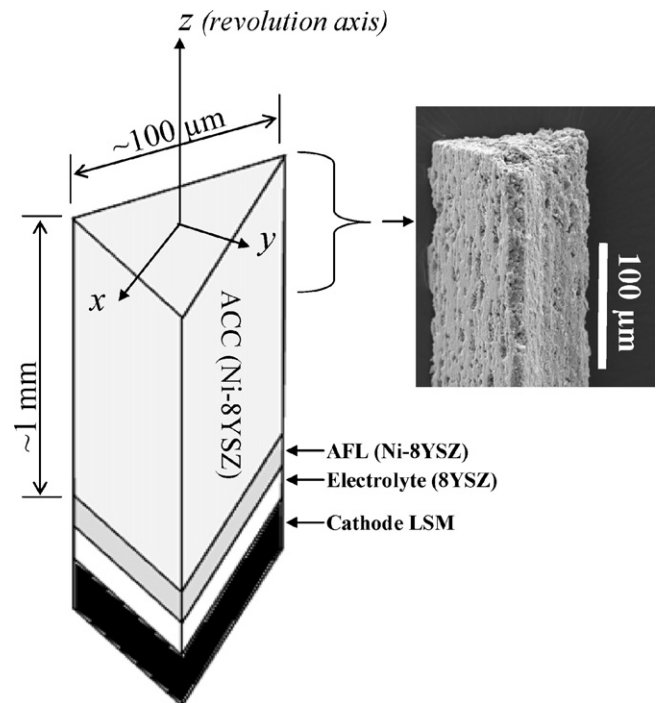
2. Experimental

2.1. Materials and sample preparation

Commercial ASC supplied by the Forschungszentrum Jülich (FZJ) research centre [4] has been used for the experiments. The anode includes a thin Anode Functional Layer (AFL) deposited on a thick Anode Current Collector (ACC). The ACC is ~ 1 mm thick and is used as the structural support of the cell. As received, the anode is constituted of 56 wt.% NiO and 44 wt.% 8YSZ (ZrO$_2$ stabilized with 8 mol% Y$_2$O$_3$). The AFL and the electrolyte (8YSZ) are thin layers of $\sim 10\,\mu m$ whereas the cathode thickness is $\sim 50\,\mu m$.

A narrow strip of cell has been prepared by laser cutting. This strip was polished up to achieve a thin plate of $100\,\mu m$ in thickness. This plate was finally sliced along the cell thickness by wire cutting to obtain the multi-layered samples for the X-ray tomography experiments. The geometry and dimensions of the samples are depicted in Fig. 1: they correspond to "needles" whose the revolution axis is perpendicular to the cell layers.

Before the tomography experiments, the samples were heated up to $T = 800\,^{\circ}C$ at a rate of $5\,^{\circ}C\,min^{-1}$ under (2%H$_2$ + Ar). They were maintained in these conditions during 48 h in order to achieve the complete reduction of NiO into Ni. This procedure has been validated by X-ray diffraction indicating that all the Ni particles are present under metallic form after the reduction treatment.

Fig. 1. Schematic representation of the samples prepared for the X-ray tomography experiments. The zoom at one extremity of the sample corresponds to a Scanning Electron Microscope (SEM) image.

The porosity of the cermet support was measured by Archimedes' method. The porosity, which is denoted ε and defined as the fraction of pores volume, was determined to $\varepsilon \sim 47\%$ for the material in its Ni–8YSZ reduced state. The specific surface area was also measured by the BET method [31]. For this purpose, pieces of cermet support (≈ 7 mm $\times$ 5 mm $\times$ 1 mm) were prepared and characterised in an Analyser SA 3100 Beckman Coulter-NG apparatus. The specific surface area, denoted S_p and defined as the surface area normalised by the pore volume, was determined for the Ni–8YSZ support to $S_p = 2.51\,\mu m^{-1}$.

2.2. X-ray tomography procedure

To produce large 3D reconstruction of SOFCs, hard X-rays must be used to prevent from excessive absorption of the beam within the sample. Given the critical dimensions of SOFCs, high resolution data are required, fostering the use of brilliant hard X-ray sources as provided by 3rd generation synchrotrons. Image acquisition has been carried out at the European Synchrotron Radiation Facility (ESRF) beamline ID22NI, based on a holotomographic scanning scheme [32]. The beam energy is fixed to 29 keV with 1.5% bandwidth. Such high energy is required to obtain a sufficient transmitted X-ray flux to investigate a large volume of material. Furthermore, this energy is high enough to get ideal phase retrieval conditions. Indeed, scans at 17 keV confirmed that, with our "thick" sample of Ni–8YSZ, the final image quality was not good enough due to the strong absorption of the X-ray beam and also because of the strong contrast in density of such porous material. The 29 keV X-ray beam is focused down to a spot below 100 nm in horizontal and vertical directions using Kirkpatrick–Baez mirrors. The beam then diverges to illuminate the sample placed downstream from the focal spot. A 2D X-ray detector is placed further downstream to record a magnified image of the sample [33,34]. In this procedure, images are not standard radiographs but rather holograms: 4 different tomographic scans at 4 sample-to-detector distances, each scan consisting of a series of 2000 projections over a turn, must be
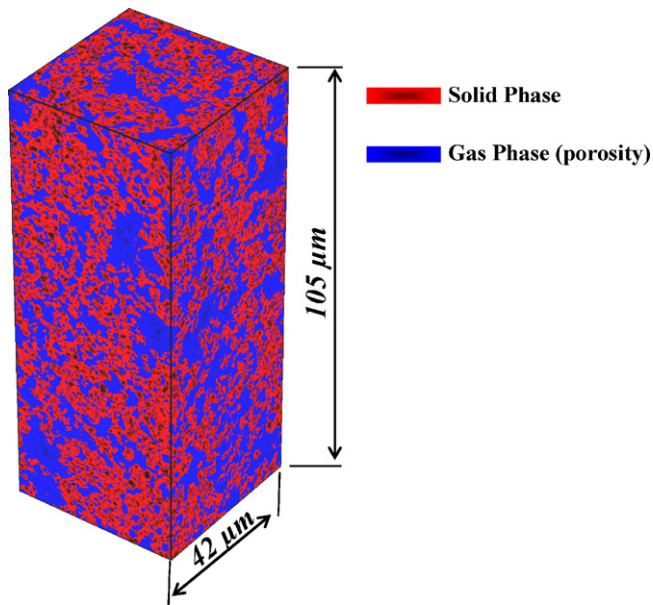
Fig. 2. Representation of the three-dimensional reconstructed microstructure of the studied Ni–8YSZ support.

Fig. 3. Porosity ε plotted as a function of the cube size ℓ extracted from the whole reconstruction.

acquired. The series of 4 tomographic scans serves as an input to a phase retrieval procedure that produces projection images whose gray levels are proportional to the projected electron density. The projected electron density images are then used as an input to a 3D volume reconstruction algorithm. The full sample imaging lasts about 90 min. The voxel size used is 60 nm, giving the field of view of about 120 μm, allowing analysing samples with cross-sections close to this value.

2.3. Three-dimensional reconstruction

In order to address the full microstructure of the Ni–8YSZ cermet, it would be required to separate the gas phase as well as the metallic and the ceramic phases of the composite. By X-ray nanotomography, Grew et al. [26] and Shearing et al. [28] have shown that this can be achieved by using differential absorption imaging across the Ni K-absorption edge (8.333 keV). However, this low beam energy is detrimental to analyse large volume due the strong absorption of the materials. For instance, Nelson et al. [35] have used cylindrical sample approximately 10 μm in diameter and 10–20 μm in height. As mentioned previously, such volumes are expected to be not large enough regarding to the coarse microstructure of SOFC support. Higher beam energy is then required. However, under this condition, Ni and 8YSZ exhibits similar X-ray absorption properties which prevent from solid phase separation.

The 3D reconstruction of the microstructure obtained in this work is illustrated in Fig. 2. A volume of 42 μm × 42 μm × 105 μm is obtained in which the solid and pore phases are identified. This reconstructed volume is located within the ACC just above the functional layer.

3. Numerical analysis: quantification of microstructure parameters

The multi-component transport in the porous cermet structure is usually modelled in the frame of the Mean Transport Pore Model (MTPM) [15,16]. This model is based on the assumption that the porous medium can be described by three microstructure parameters: the porosity, the tortuosity factor and the mean pore radius.
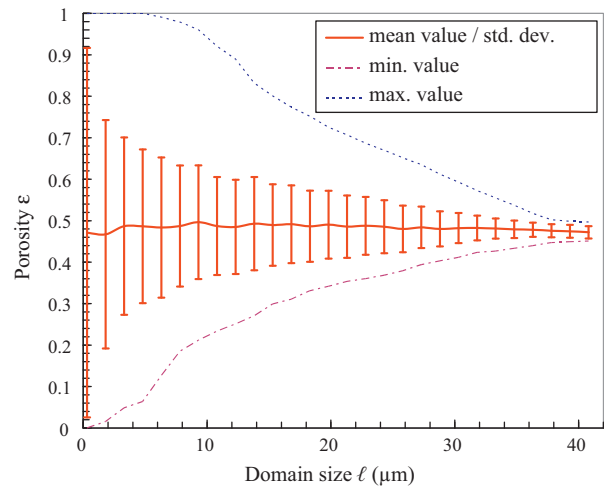
This section of the paper is focused on the determination of these three structural parameters from the 3D reconstruction.

3.1. Fluid contiguity and porosity

The connectivity of the gas phase can be represented by the fluid contiguity which is defined by the volumetric percentage of the connected pores [26]. An in-house program has been implemented in the commercial Matlab® software to calculate this parameter. The program has been developed by fulfilling the following rules: two voxels of pores, that shared one common face, were considered as connected to form a cluster; whereas two voxels only linked by an edge or a vertex were considered as disconnected. As described in Ref. [26], the percolating volume of pores was then identified by removing from the network the isolated clusters which are either embedded as closed porosity in the bulk or emerge only at one edge of the 3D reconstruction. The 3D pores network of the reduced cermet has been characterised by this method. The numerical analysis has revealed that 96% of the pore phase is percolating. This result means that the main part of the pores is connected in one single network, suggesting that the porous medium exhibits a good ability regarding the gas flow.

Porosity has been also determined for a set of sub-volumes, which have been randomly extracted from the whole 3D reconstruction. These sub-volumes correspond to cubes for which the edge length ℓ ranges from 0.3 μm to 40.8 μm. Considering domains with the same size ℓ, a sufficient large number of analyses allows determining the average porosity and its standard deviation. The mean porosity is given in Fig. 3 and agrees the value provided by the Archimedes' method (i.e. 47%: see Section 2.1). This result tends to confirm the accuracy of the reconstruction.

As illustrated in Fig. 3, the standard deviation from the mean porosity value decreases with increasing the volume size. The dispersion becomes negligible for volume higher than 35 μm × 35 μm × 35 μm. In other words, this volume is sufficiently large to be statistically representative of the heterogeneous material and can be taken as the threshold corresponding to the Representative Volume Element (RVE) for the investigated property.

3.2. Surface area and mean pore radius

The specific surface area is defined as the surface area normalised by the phase volume [18]. This parameter has been calculated for the porosity. For this purpose, each voxel face of the
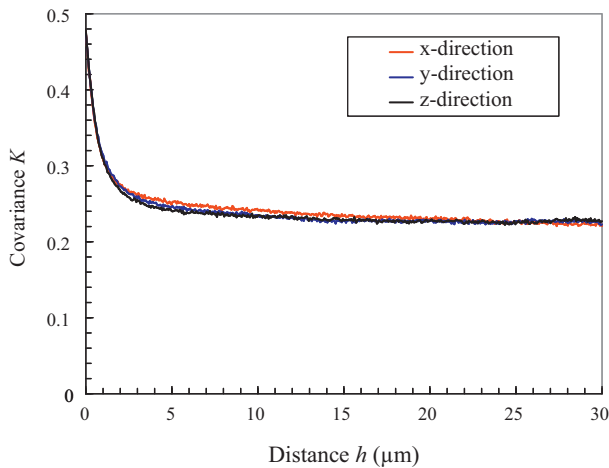
Fig. 4. Covariograms calculated from the 3D reconstruction. The covariance K has been computed in the x, y, z directions.

Fig. 5. Schematic representation of sinuous but parallel pores to define the tortuosity.

3D reconstruction has been examined: interfaces between solid and gas have been identified and then enumerated in order to calculate the fluid/solid area thanks to the surface of the voxel face (i.e. ℓ_{voxel}^2). It is worth noting that the value calculated by this method requires a rescaling in order to estimate the real surface. Indeed, as the structure is described by cubic elements (i.e. the voxels), the surface of objects included in the digitized reconstruction is overestimated [36]. Under simple geometrical considerations, it can be shown that the scaling corresponds to a factor of $\pi/6$, if the objects are spherical or randomly oriented (indeed, in this case, the factor is equal to the ratio between the surfaces of a sphere and a cube). As a consequence, it can be reasonably supposed the real specific pore surface area ranges between the rough data deduced directly from the numerical reconstruction and the processed value obtained after the scaling by a factor $\pi/6$: $1.80\,\mu\text{m}^{-1} < S_p < 3.45\,\mu\text{m}^{-1}$. It worth noting that the median value, i.e. $2.62\,\mu\text{m}^{-1}$, is found to be in good agreement with the data estimated by the BET method, i.e. $2.51\,\mu\text{m}^{-1}$ (see Section 2.1).

It is assumed that an assemblage of spherical pores (all with the same size) is representative for the material porosity. In this case, the specific surface area can be linked to the mean pore radius R_p according to [37]:

$$S_p = \frac{3}{R_p} \tag{1}$$

This relation leads to determine an average pore diameter of $2 \times R_p = 2.4\,\mu\text{m}$. In order to check this value, the covariogram $K(h)$ of the reconstruction has been computed from the reconstruction [38]. It can be expressed as a measure of the intersection between the porosity of the material and its image after a translation h of the medium. Considering the x-direction, K can be written as followed:

$$K(h) = \frac{1}{V} \int k(x,y,z) \times k((x+h),y,z) \times dV,$$
$$\text{with} \quad k(x) = \begin{cases} 1 & \text{if } x \text{ belongs to the pore phase} \\ 0 & \text{if } x \text{ is in the solid phase} \end{cases} \tag{2}$$

Based on the 3D tomographic images, covariograms have been computed in the three directions and are provided in Fig. 4. As expected, $K(h)$ is equal to the value of the porosity for $h = 0$ and tends to an asymptotic theoretical value corresponding to the square of the porosity: $\lim_{h\to\infty} K(h) = \varepsilon^2$ [38]. The distance h^* to reach this limit corresponds to the range of the covariance and can be ascribed to the characteristic length of the porosity [38]. A criterion chosen as $((K(h^*) - \varepsilon^2)/\varepsilon^2) \leq 0.05$ leads to an estimation of the characteristic
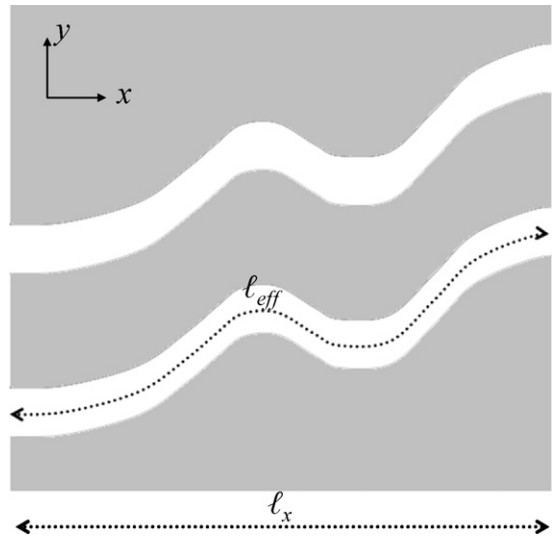
size for the pores of $h^* \sim 3\,\mu\text{m}$. This value is consistent with the mean pore diameter $2R_p$ assessed previously by assuming a packing of spherical pores. As a consequence, it can be concluded that the mean pore radius of the analysed substrate ranges between 1.2 and 1.5 μm.

3.3. Tortuosity factor

Definition and numerical method – Tortuosity ζ can be calculated for the three directions of the 3D reconstruction. For the sake of simplicity, this parameter can be easily expressed considering a 2D representation as depicted in Fig. 5. In this case, the tortuosity is defined as the ratio between the effective path length ℓ_{eff} and the length of the sample ℓ_x (Fig. 5):

$$\zeta_x = \frac{\ell_{eff}}{\ell_x} \tag{3}$$

Considering a porous medium as a bundle of sinuous but parallel capillaries, it can be demonstrated that the fluid effective diffusion coefficient D_i^{eff} is given by [39]:

$$D_i^{eff} = \frac{\varepsilon}{\tau_i} D_{bulk} \quad \text{with} \quad \tau_i = \left(\frac{\ell_{eff}}{\ell_i}\right)^2$$
$$i = \text{bundle-direction} \ (x, y \text{ or } z) \tag{4}$$

The term τ_i is usually named as the tortuosity factor and D_{bulk} denotes the diffusion coefficient of the gas. In porous materials such as SOFC electrodes, there are many pathways that are entangled together. For this reason, it is impossible and not relevant to define an effective transport path length, ℓ_{eff}, and hence, a "geometrical" tortuosity ζ of the medium [22,39]. In other terms, the effective diffusion coefficient cannot be determined from geometrical considerations. However, provided that D_i^{eff} can be calculated by other methods, it becomes possible to calculate the empirical ratio of the porosity to a "reliable tortuosity factor", $(\varepsilon/\tau_i) = (D_i^{eff}/D_{bulk})$, which takes into account the effects of structure.

Several methods have been proposed to evaluate the tortuosity factor through the calculation of an effective diffusion coefficient. The tortuosity factor can be calculated by using the Lattice Boltzman Method (LBM) [20,26]. Iwai et al. [20,22] have statistically calculated this parameter from the random walk process. Wilson
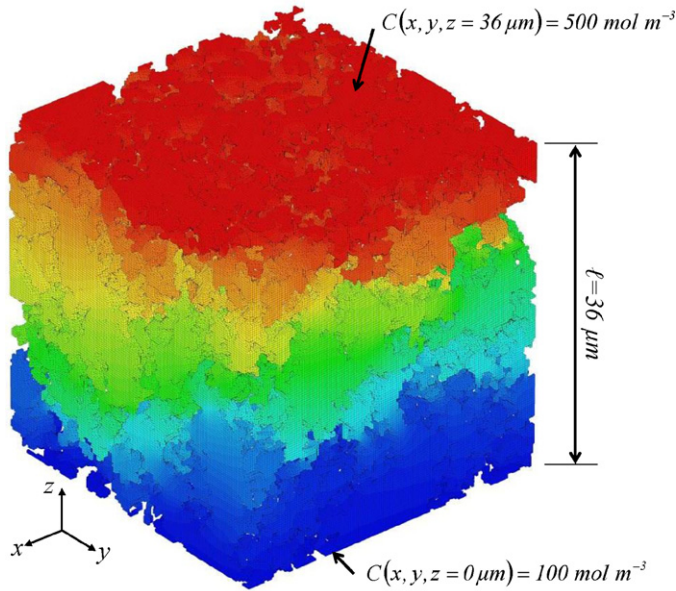
Fig. 6. Concentration field in the percolated porosity (volume of $36\,\mu m \times 36\,\mu m \times 36\,\mu m$ extracted from the 3D reconstruction, two concentrations imposed at $z = 0$ and $z = 36\,\mu m$ as boundary condition, Element (or voxel) size $\ell_{voxel} = 240\,nm$, 2.2×10^6 nodes).

et al. [17] and Joos et al. [24,40] have solved the Laplace's equation for diffusion within the microstructure by using the Finite Element Method (FEM). Although the boundary conditions chosen for these simulations can introduce a bias in the assessment of the effective property [38], this effect has not been estimated for SOFC electrode yet.

In this work, mass transfer by diffusion in the gas phase of the microstructure has been simulated by FEM. The Cast3M solver [41] has been used for this purpose. The mesh has been built by converting each voxel of the open porosity into an 8-nodes cubic element. Thanks to the methodology used to identify the percolated gas phase (see Section 3.1), no element can be connected to a neighbour by an edge or a vertex. This method prevents from reducing locally to zero the size of the section for gas transport which would act as a geometrical singularity in the mesh.

Only cubic volumes extracted from the reconstruction have been analysed in order to avoid any anisotropic dimensional effect on the result. Simulations have been carried out by imposing a uniform concentration or molar flux onto two opposite faces of the domain (*i.e.* the opposite external faces of the cube perpendicular to the three x, y or z axes). In the other part of the mesh, no boundary condition has been applied. It can be noticed that this condition is equivalent to obtain a zero molar flux through the solid/gas interface in the real sample. Over the modelled structure, the Laplace's equation for diffusion is solved by the FEM:

$$div\left[-D_{bulk} \times gradC\right] = 0 \Leftrightarrow -D_{bulk}\left\{\frac{\partial^2 C}{\partial x^2} + \frac{\partial^2 C}{\partial y^2} + \frac{\partial^2 C}{\partial z^2}\right\} = 0 \quad (5)$$

where C is the concentration at the location (x, y, z) and D_{bulk} is supposed independent of C. As an illustration, a simulated concentration field in the percolated porosity is plotted in Fig. 6 for a volume of $36\,\mu m \times 36\,\mu m \times 36\,\mu m$ extracted of the cermet reconstruction. It can be noticed that the mesh for this simulation contains 2.2×10^6 nodes.

Once the concentration field is known, the effective diffusion coefficient can be easily deduced from the net flux N_i entering or
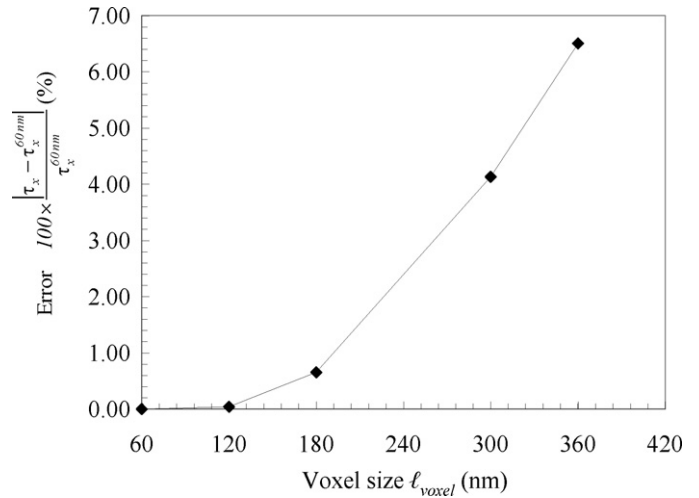
Fig. 7. Error on the tortuosity factor τ_x versus the voxel size. Simulations performed for a volume of $9\,\mu m \times 9\,\mu m \times 9\,\mu m$ and two concentrations imposed at $x = 0$ and $x = 9\,\mu m$ as boundary condition.

exiting from the domain:

$$\frac{N_i}{\Delta j \Delta k} = -D_i^{eff}\frac{\langle C_{i=\Delta i}\rangle - \langle C_{i=0}\rangle}{\Delta i} \quad \text{with } \langle C_i\rangle$$

$$= \frac{1}{\Delta j \Delta k}\int_s C_i \times ds \quad (i = x, y \text{ or } z; \ j \neq i \text{ and } k \neq i, j) \quad (6)$$

where $\Delta j = \Delta k = \Delta i = \ell$ is the edge length of the simulated cubic volume and S its surface ($S = \ell^2$). The tortuosity factor is then determined by combining Eqs. (4) and (6).

Sensitivity analysis – A sensitivity analysis has been performed on the tortuosity factor by changing either the voxel size ℓ_{voxel} or the simulated volume length ℓ. A specific procedure has been implemented in Matlab® to decrease the resolution of the 3D reconstruction. In the method, a cube of n^3 ($n = 2, 3, 4, \ldots$) initial voxels have been merged together to form a new cubic element. In the case where such a coarse voxel contained sub-voxels belonging to the solid and pore phases, the nature of the new element was determined as followed: it was attributed to the gas phase when the pore sub-voxels were predominant within the initial set of sub-voxels. Conversely, when they were found in minority, the new element was considered belonging to the solid phase. In case of strict equality, the nature of the element was chosen randomly.

The voxel size dependence has been investigated on a volume of $9\,\mu m \times 9\,\mu m \times 9\,\mu m$ extracted from the 3D reconstruction. The simulations have been carried out to calculate the tortuosity factor τ_x according to the x-direction. Two uniform concentrations have been imposed on the left and right surfaces of the modelled volume respectively at $x = 0\,\mu m$ and $x = 9\,\mu m$. In Fig. 7, the error on the tortuosity factor has been plotted as a function of the voxel length. It can be seen that the size of the discretization must be lower than $\ell_{voxel} \leq 300\,nm$ to avoid any error higher than $100 \times \left|\tau_x - \tau_x^{\ell voxel=60\,nm}\right|/\tau_x^{\ell voxel=60\,nm} \geq 4.1\%$. It has been checked that this result remains valid for the tortuosity factors, τ_y and τ_z, determined according to the y- and z-direction. It is worth noting that this criterion will be fulfilled for all the simulations presented in subsequent part of this article.

The tortuosity factors have been also calculated by increasing the simulated domain from $9\,\mu m \times 9\,\mu m \times 9\,\mu m$ up to $41.4\,\mu m \times 41.4\,\mu m \times 41.4\,\mu m$. In this studied case, it can be noticed the porosity decreases with increasing investigated volumes from $\sim 55\%$ down to $\sim 47\%$. Simulations have been performed by imposing two uniform concentrations at the boundaries. Results are plotted in Fig. 8. It is found that the values become steady for
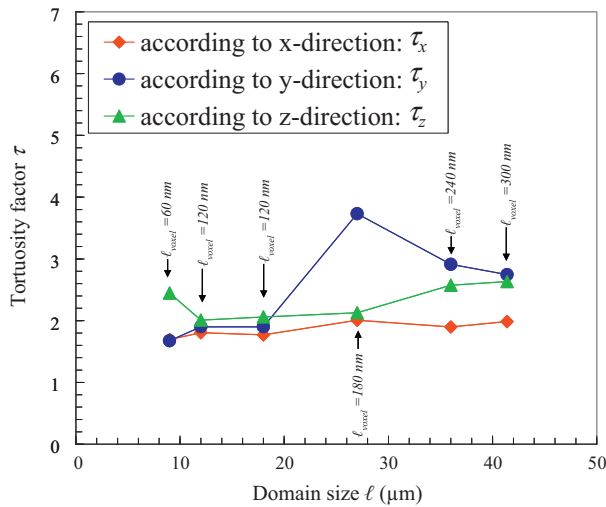
Fig. 8. Tortuosity factors τ_x, τ_y, τ_z plotted as a function of the modelled volume length ℓ. The label gives the size of the voxels, ℓ_{voxel}, for which the mesh has been built. Simulations have been performed for two imposed concentrations at boundary (*i.e.* the opposite surface of the domain).

Table 1
Tortuosity factors calculated for three disconnected volumes of $36 \,\mu m \times 36 \,\mu m \times 36 \,\mu m$ extracted from the 3D reconstruction (uniform concentration imposed at boundary, $\ell_{voxel} = 240$ nm).

	Zone no. 1	Zone no. 2	Zone no. 3	Mean value
τ_x	1.9	2.5	2.5	2.3
τ_y	2.9	2.8	2.6	2.8
τ_z	2.6	2.7	2.6	2.6

volumes larger than $35 \,\mu m \times 35 \,\mu m \times 35 \,\mu m$. This result means that the size of the RVE relevant for the tortuosity factor is close to the one required for the porosity. As a consequence, this volume can be considered as a threshold from which the reconstruction becomes statistically representative for the porous cermet support.

Spatial averaging – The tortuosity factors τ_x, τ_y and τ_z have been computed for three volumes of $36 \,\mu m \times 36 \,\mu m \times 36 \,\mu m$ taken at different location along the height of the 3D reconstruction (*i.e.* according to the vertical *z*-axis). It is worth noting that the extracted domains are disconnected from one to each other. The simulations have carried out by imposing two uniform concentrations at the boundaries.

The values of the tortuosity factors in each direction are reported in Table 1. It can be noticed that the scattering on τ_x, τ_y or τ_z values is narrow, *i.e.* the tortuosity factors do not depend on the location of the analysed volume in the support. This result confirms that

volumes as large as $35 \,\mu m \times 35 \,\mu m \times 35 \,\mu m$ are required to determine the effective transport properties of the Ni–YSZ substrate.

Moreover, a slight difference is noticeable between τ_x, τ_y and τ_z with a similar trend for the three modelled volumes: $\tau_y \geq \tau_z \geq \tau_x$. It can be inferred from this result that the medium presents a slight anisotropy regarding to the diffusion of gaz.

Effect of boundary conditions – The impact of boundary conditions has been investigated for the three following cases depicted in Table 2:

(i) The first case has been used in the previous section: two uniform concentrations are imposed on the opposite surfaces of the volume (at $z = 0$ and $z = \ell$).
(ii) The second case corresponds to an intermediate boundary condition where one uniform concentration is imposed on the lower surface (at $z = 0$) and a flux is applied on the upper surface (at $z = \ell$).
(iii) In the last condition, two fluxes are applied on the lower and upper surfaces of the analysed cube. It can be noticed that, in this case, the concentration on one point of the structure needs to be defined.

The results on τ_z are summarized in Table 2. Although the simulated volume is slightly higher than the estimated RVE (*i.e.* $35 \,\mu m \times 35 \,\mu m \times 35 \,\mu m$), the three investigated cases lead to a significant difference on the tortuosity factor. This phenomenon is caused by some edged effects which arise when the boundary conditions are applied on a limited domain [38]. From a theoretical point of view, these effects must vanish for an infinite volume, where surfaces of isoconcentration values can be considered to be plane and perpendicular to the cube edges. A close examination of Fig. 6 shows that it is not the case at the scale of the analysed volume. In practice, the first and the last cases give respectively a lower and upper bound for the tortuosity factor. Furthermore, it can be noticed that the intermediate case corresponds to the closest conditions regarding to the SOFC application. Indeed, the hydrogen electro-oxidation controls the H_2 and H_2O fluxes at the anode/electrolyte interface; whereas the fuel flowing along the gas distributor imposes the concentrations at the other side of the cermet. As a consequence, it can be proposed to use in SOFC models a tortuosity factor of $\tau_z = 2.8$ for the cermet support (with a upper bound of $\tau_z^{max} = 3.1$ and a lower bound of $\tau_z^{min} = 2.6$ denoted $\tau_z = 2.8_{-0.2}^{+0.3}$).

4. Discussion

RVE size and voxel resolution – Since they control the diffusion in the thick substrate, the morphological properties of SOFC supports constitute key parameters regarding to the optimisation of SOFCs performance. A methodology is proposed in this paper to assess

Table 2
Tortuosity factors calculated considering three different boundary conditions (volumes of $36 \,\mu m \times 36 \,\mu m \times 36 \,\mu m$ and $\ell_{voxel} = 240$ nm).

(i) Two concentrations imposed at $z = 0$ and $z = 36 \,\mu m$	(ii) One concentration imposed at $z = 0$ and one flux imposed at $z = 36 \,\mu m$	(iii) Two fluxes imposed at $z = 0$ and $z = 36 \,\mu m$
τ_z 2.6	2.8	3.1
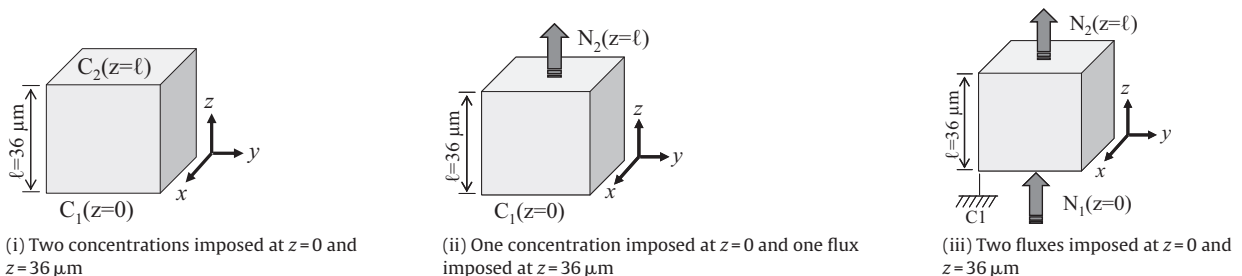
these parameters in the frame of a 3D reconstruction obtained from nano-tomography measurements. Applied on a commercial Ni–YSZ support, it has been shown that bigger volumes than the ones considering for the functional electrodes need to be analysed. Indeed, reconstruction as large as $35\,\mu m \times 35\,\mu m \times 35\,\mu m$ is required to be statistically representative of the whole substrate regarding to the fluid properties. Moreover, it is found that the ratio between the size of the RVE and the mean pore diameter is equal to $(\ell_{RVE}(=35\,\mu m)/\langle 2R_p \rangle (=2.4\,\mu m))=14.6$. This result is consistent with the conclusion established by Metcalfe et al. [30] who have found on the basis of a purely numerical study that "a cubic envelope having a minimum length of 14 times the mean particle diameter was necessary to adequately represent the electrode structure".

Conversely to the size of the RVE, the resolution of the 3D reconstruction appears to be less important, given that a voxel size of $60\,nm \times 60\,nm \times 60\,nm$ is largely sufficient to describe accurately the porosity phase. Indeed, in the studied case, the microstructure is relatively coarse in comparison to the functional electrode. Considering the mean pore diameter $\langle 2R_p \rangle = 2.4\,\mu m$, one characteristic void of the material will be depicted in one direction by 40 elements of 60 nm or 10 elements of 240 nm (leading respectively to ~33,510 and ~523 voxels included in the pore volume). Therefore, both the RVE size and the resolution of the reconstruction are consistent with the characteristic length of the microstructure. As a consequence, the methodology based on hard X-ray nano-tomography experiments appears to be well adapted to investigate SOFCs support. Indeed, this method allows investigating large volumes at intermediate resolution. Conversely, the 3D reconstructions based on the FIB-SEM technique would not be suitable, because (i) the examination of large volumes is time-expensive and (ii) the high resolution provided by this technique is not necessary. As a conclusion, it is proposed to use the hard X-ray nano-tomography experiments to obtain reconstruction from SOFCs support; whereas the FIB-SEM technique can be restricted to obtain reconstruction of the functional electrodes.

Tortuosity factor – It has been proposed in Section 3.3 to determine the value of the tortuosity factor with the intermediate boundary conditions depicted in Table 2: this condition corresponds to one flux and one concentration imposed as boundary conditions and leads to $\tau_z = 2.8^{+0.3}_{-0.2}$. This value is bounded by an upper and lower values corresponding to the first and the third boundary conditions given in Table 2 (*i.e.* 2 concentrations or 2 fluxes imposed). In other word, the tortuosity factor is determined with an error of $+11\%/-7\%$. Therefore, although it is not discussed elsewhere for SOFC application, it is worth underlining that the calculated effective properties of porous electrodes has to be determined by estimating the bias introduced by the choice of the boundary conditions.

It can be noticed that the tortuosity factors determined in the present study are slightly higher than the values reported in literature for Ni–YSZ electrodes. For instance, Wilson et al. [17] and Iwai et al. [20] have obtained respectively $(\tau_x, \tau_y, \tau_z) = (2.1, 2.2, 1.9)$ and $(\tau_x, \tau_y, \tau_z) = (2.03, 2.06, 1.83)$; whereas Grew et al. [26] have found $(\tau_x, \tau_y, \tau_z) = (1.77, 1.51, -)$. These discrepancies in the results can be first of all attributed to the difference in microstructures and layer thicknesses between the cermet used as a "functional" electrodes or a cell support. It can be also mentioned that, in our case, the "non-steady" tortuosity factor decreases with decreasing the size of the analysed volume (for volume lower than the RVE) before reaching the steady value (Fig. 8). For example, an "non-steady" tortuosity factor of $\tau_z = 2.01$ is obtained on a volume of the reconstruction limited at $12\,\mu m \times 12\,\mu m \times 12\,\mu m$.

Isotropy of the microstructure – As shown in Fig. 4, the covariograms $K(h)$ computed in the three directions of the space are very similar. That means that the characteristic dimensions of the pores are equal whatever the considered direction and suggests that the shape of the voids is isotropic. This result justifies the assumption taken in Section 3.2 to describe the gas phase by an assemblage of spherical pores. Nevertheless, the slight difference in tortuosity factors (see Table 2) could indicate that the medium exhibits a slight anisotropy in the percolated pathways for the gas diffusion.

If we consider now the medium composed by an assemblage of mono-sized solid spheres, the tortuosity factor τ for the gas phase is given by the following expression [42]:

$$\tau = \left(1.23 \frac{(1-\varepsilon)^{4/3}}{\varepsilon} \right)^2 \qquad (7)$$

The use of this equation leads to a tortuosity factor of only $\tau = 1.26$ for $\varepsilon = 0.47$. It can be mentioned that this value is in good agreement with the ones simulated by Zalc et al. [43] for spheres packing with the same void fraction. However, this value is much lower than the one measured in this work. It is suggested that the topology of the solid phase is poorly described by a packing of solid spherical particles for the studied cermet. Rather, solid phase in Ni–YSZ cermets may be better represented by a continuous "skeleton" embedding spherical pores. In such pores network, some constriction effects may rise the value of the tortuosity [43].

5. Conclusion

A methodology has been proposed in this work to obtain 3D reconstruction of porous SOFC supports. Synchrotron X-ray nano-tomography measurements have been carried out on commercial Ni–8YSZ cermet. The beam energy has been selected at 29 keV in order to obtain simultaneously (i) the required high transmitted X-ray flux and (ii) the optimised solid/void phase retrieval conditions. Thanks to this experimental procedure, a large volume of the porous material has been inspected. A 3D reconstruction of $42\,\mu m \times 42\,\mu m \times 105\,\mu m$ has been obtained with a voxel resolution of 60 nm.

The 3D reconstruction has been numerically analysed. A good isotropy of the microstructure has been highlighted by calculating the covariograms in the three directions of the reconstruction. Considering the morphological properties controlling the gas diffusion, it has been shown that a volume as large as $35\,\mu m \times 35\,\mu m \times 35\,\mu m$ is required to be statistically representative of the whole support. A porosity of $\varepsilon = 47\%$ and a mean pore radius of $\langle R_p \rangle = 1.2\,\mu m$ have been found for the studied Ni–8YSZ cermet. The tortuosity factor τ has been also calculated on the basis of finite element simulations performed on the 3D reconstruction. It has been shown that, even for a computed volume of $36\,\mu m \times 36\,\mu m \times 36\,\mu m$, the value for the tortuosity factor is not completely independent of the boundary conditions chosen for the simulations. In this condition, it is proposed to determine the tortuosity factor for an intermediate boundary condition which is relevant for SOFC application. The lower and upper limit of this parameter can also be specified by considering two uniform concentrations or flux as boundaries conditions. By using this approach, the tortuosity factor of the studied cermet has been determined in the direction perpendicular to the anode/electrolyte interface to $\tau_z = 2.8^{+0.3}_{-0.2}$.

References

[1] F. Tietz, H.P. Buchkremer, D. Stöver, Solid State Ionics 152–153 (2002) 373–381.
[2] N.H. Menzler, F. Tietz, S. Uhlenbruck, H.P. Buchkremer, D. Stöver, J. Mater. Sci. 45 (2010) 3109–3135.
[3] W.Z. Zhu, S.C. Deevi, Mater. Sci. Eng. A 362 (2003) 228–239.
[4] R.N. Basu, G. Blass, H.P. Buchkremer, D. Stöver, F. Tietz, E. Wessel, I.C. Vinke, J. Eur. Ceram. Soc. 25 (2005) 463–471.
[5] J. Laurencin, F. Lefebvre-Joud, G. Delette, J. Power Sources 177 (2008) 355–368.
[6] J. Mizusaki, H. Tagawa, K. Tsuneyoshi, A. Sawata, J. Electrochem. Soc. 138 (7) (1991) 1867–1873.
[7] A.V. Virkar, J. Chen, C.W. Tanner, J.-W. Kim, Solid State Ionics 131 (2000) 189–198.
[8] Q. Cai, C.S. Adjiman, N.P. Brandon, Electrochem. Acta 56 (2011) 5804–5814.
[9] D. Simwonis, F. Tietz, D. Stöver, Solid State Ionics 132 (2000) 241–251.
[10] T. Matsui, R. Kishida, J.-Y. Kim, H. Muroyama, K. Eguchi, J. Electrochem. Soc. 157 (5) (2010) B776–B781.
[11] J.R. Wilson, J.S. Cronin, S.A. Barnett, Scr. Mater. 65 (2011) 67–72.
[12] H. Sumi, R. Kishida, J.-Y. Kim, H. Muroyama, T. Matsui, K. Eguchi, J. Electrochem. Soc. 157 (12) (2010) B1747–B1752.
[13] J.W. Kim, A.V. Virkar, K.Z. Fung, K. Metha et, S.C. Singhal, J. Electrochem. Soc. 146 (1) (1999) 69–78.
[14] J. Laurencin, D. Kane, G. Delette, J. Deseure, F. Lefebvre-Joud, J. Power Sources 196 (2011) 2080–2093.
[15] T. Ackmann, L.G.J. de Haart, W. Lehnert, D. Stolten, J. Electrochem. Soc. 150 (6) (2003) A783–A789.
[16] W. Lehnert, J. Meusinger, F. Thom, J. Power Sources 87 (2000) 57–63.
[17] J.R. Wilson, W. Kobsiriphat, R. Mendoza, H.-Y. Chen, J.M. Hiller, D.J. Miller, K. Thornton, P.W. Voorhees, S.B. Adler, S.A. Barnett, Nat. Mater. 5 (2006) 541–544.
[18] J.R. Wilson, J.S. Cronin, A.T. Duong, S. Rukes, H.-Y. Chen, K. Thornton, D.R. Mumm, S. Barnett, J. Power Sources 195 (2010) 1829–1840.
[19] J.S. Cronin, J.R. Wilson, S.A. Barnett, J. Power Sources 196 (5) (2011) 2640–2643.
[20] H. Iwai, N. Shikazono, T. Matsui, H. Teshima, M. Kishimoto, R. Kishida, D. Hayashi, K. Matsuzaki, D. Kanno, M. Saito, H. Muroyama, K. Eguchi, N. Kasagi, H. Yoshida, J. Power Sources 195 (2010) 955–961.
[21] P.R. Shearing, J. Golbert, R.J. Chater, N.P. Brandon, Chem. Eng. Sci. 64 (2009) 3928–3933.
[22] M. Kishimoto, H. Iwai, M. Saito, H. Yoshida, J. Power Sources 196 (10) (2011) 4555–4563.
[23] N. Vivet, S. Chupin, E. Estrade, T. Piquero, P.L. Pommier, D. Rochais, E. Bruneton, J. Power Sources 196 (2011) 7541–7549.
[24] J. Joos, T. Carraro, A. Weber, E. Ivers-Tiffée, J. Power Sources 196 (17) (2011) 7302–7307.
[25] D. Kanno, N. Shikazono, N. Takagi, K. Matsuzaki, N. Kasagi, Electrochem. Acta 56 (2011) 4015–4021.
[26] K.N. Grew, Y.S. Chu, J. Yi, A.A. Peracchio, J.R. Izzo, Y. Hwu, F. De Carlo, W.K.S. Chiu, J. Electrochem. Soc. 157 (6) (2010) B783–B792.
[27] P.R. Shearing, J. Gelb, N.P. Brandon, J. Eur. Ceram. Soc. 30 (2010) 1809–1814.
[28] P.R. Shearing, J. Gelb, J. Yi, W.-K. Lee, M. Drakopolous, N.P. Brandon, Electrochem. Commun. 12 (2010) 1021–1024.
[29] G.J. Nelson, W.M. Harris, J.J. Lombardo, J.R. Izzo, W.K.S. Chiu, P. Tanasini, M. Cantoni, J. Van Herle, C. Comminellis, J.C. Andrews, Y. Liu, P. Pianetta, Y.S. Chu, Electrochem. Commun. 13 (2011) 586–589.
[30] C. Metcalfe, O. Kesler, T. Rivard, F. Gitzhofer, N. Abatzoglou, J. Electrochem. Soc. 157 (9) (2010) B1326–B1335.
[31] S. Brunauer, P.H. Emmet, E. Teller, J. Am. Chem. Soc. 60 (1938) 309–319.
[32] P. Cloetens, W. Ludwig, J. Baruchel, D. Van Dyck, J. Van Landuyt, J.P. Guigay, M. Schlenker, Appl. Phys. Lett. 75 (19) (1999) 2912–2914.
[33] P. Bleuet, P. Cloetens, P. Gergaud, D. Mariolle, N. Chevalier, R. Tucoulou, J. Susini, A. Chabli, Rev. Sci. Instrum. 80 (2009) 056101-1–056101-3.
[34] R. Mokso, P. Cloetens, E. Maire, W. Ludwig, J.-Y. Buffière, Phys. Lett. 90 (14) (2007) 144104-1–144104-3.
[35] G.J. Nelson, J.R. Izzo, J.J. Lombardo, W.M. Harris, A.P. Cocco, W.K.S. Chiu, K.N. Grew, A. Faes, A. Hessler-Wyser, J. Van Herle, Y.S. Chu, S. Wang, ECS Trans. 35 (1) (2011) 1323–1327.
[36] D.A. Rajon, P.W. Patton, A.P. Shah, C.J. Watchman, W.E. Bolch, Med. Phys. 29 (2002) 682–693.
[37] K.S.W. Sing, in: G.D. Parfitt, K.S.W. Sing (Eds.), Characterization of Powder Surfaces, Academic Press, 1976.
[38] T. Kanit, S. Forest, I. Galliet, V. Mounoury, D. Jeulin, Int. J. Solids Struct. 40 (2003) 3647–3679.
[39] N. Epstein, Chem. Eng. Sci. 44 (3) (1989) 777–789.
[40] B. Rüger, J. Joos, A. Weber, T. Carraro, E. Ivers-Tiffée, ECS Trans. 25 (2) (2009) 1211–1220.
[41] http://www-cast3m.cea.fr/.
[42] P.-Y. Lanfrey, Z.V. Kuseljevic, M.P. Dudukovic, Chem. Eng. Sci. 65 (2010) 1891–1896.
[43] J.M. Zalc, S.C. Reyes, E. Iglesia, Chem. Eng. Sci. 58 (2003) 4605–4617.